Wear 586 (2026) 206457

Contents lists available at ScienceDirect

Wear

journal homepage: www.elsevier.com/locate/wear

Amorphous $CaSO_4$ nanocrystal deposits for friction and wear reduction at silicon interfaces

Tijn Vernooij [a,b], H. Tunç Çiftçi [a], Noushine Shahidzadeh [c], Bart Weber [a,c,*]

[a] Advanced Research Center for Nanolithography (ARCNL), Science Park 106, 1098 XG Amsterdam, The Netherlands
[b] Institute for Theoretical Physics, Institute of Physics, University of Amsterdam, Science Park 904, 1090 GL Amsterdam, The Netherlands
[c] Van der Waals-Zeeman Institute, Institute of Physics, University of Amsterdam, Science Park 904, 1098 XH Amsterdam, The Netherlands

ARTICLE INFO

Keywords:
Amorphous calcium sulfate nanocrystals
Sacrificial coatings
Atomic force microscopy
Precision positioning systems
Semiconductor manufacturing
Solid lubricants

ABSTRACT

When an object is placed on a surface, friction and wear cause uncertainty in its exact position, and thus challenge precision manufacturing. Here, we explore the development of a sacrificial nanocrystal deposit that can suppress friction and wear. Amorphous $CaSO_4$ nanocrystals are deposited through salt solution droplet deposition followed by evaporation. During droplet drying, a precursor film of the aqueous $CaSO_4$ solution spreads onto a hydrophilic silicon wafer, thus nucleating evenly spread unfaceted amorphous nanocrystals of $CaSO_4$ on the wafer surface. We used atomic force microscopy to study the extent, topography, and friction and wear behavior of the deposited nanocrystals. We find that the sacrificial layer of nanocrystals is easy to apply and remove, spreads over large (few cm) areas with a constant thickness of about 8 nm, and has favorable friction and wear behavior.

1. Introduction

In many areas of science and engineering, the ability to precisely locate samples on a positioner surface relative to a reference point is vital to maintaining experimental precision and repeatability [1,2]. When (sub)nanometer-scale precision is needed, friction and wear at the interface between the sample and the positioner can cause significant challenges [3]. During repeated placement and removal of samples on a positioner surface, wear of the positioner may occur, even when the positioner surface is harder than the sample [4]. Wear can cause uncertainty in the exact location and orientation of subsequent samples placed on the same positioner surface, reducing positioner performance and lifetime.

Hard ceramics are currently the standard choice for components that need to be highly resistant to wear [5–7]. However, even the hardest ceramics wear after repeated contact with softer materials [4,8,9], such as silicon. Therefore, alternative or additional approaches towards wear suppression are desired.

Salt crystals can be of interest in the context of friction and wear control because salt crystals are stiff and can be easily grown and removed. The crystalization pressure of NaCl exceeds the tensile strength of many types of porous stones. As a result, salt crystallization is a major pathway for the degradation of rock and human-made structures [10–13]. At the same time, sliding on NaCl and similar salts can involve relatively low friction coefficients of around 0.1 [14–16]. Materials reinforced with $CaSO_4$ whiskers generally have lower friction and higher wear resistance [17,18], while solid $CaSO_4$ performs well as a high temperature lubricant [19,20]. At the same time, ceramic materials wear slower when sliding against lower hardness materials, such as salts [21,22]. Gypsum has an indentation hardness of just 1 to 1.5 GPa [23,24] compared to about 10 GPa for silicon [4]. All these previous studies suggest that deposits made of relatively softer salts can protect a ceramic positioner surface from wear while also lowering friction.

Here, we investigate if a deposit of $CaSO_4$ nanocrystals [25] applied to naturally oxidized, polished silicon surfaces can reduce friction and wear at the interface between silicon surfaces. In order to grow $CaSO_4$ nanocrystals on the silicon surface, a droplet ($V=1\,\mu L$) of nearly saturated $CaSO_4$ solution is deposited at the oxygen plasma cleaned surface, followed by drying at $T = 21\,°C$ and RH = 30%–50%. The evaporation, which leads to crystallization of the salt, results in a homogeneous deposit of amorphous $CaSO_4$ nanocrystals in the precursor wetting film of the doplet [26,27]. The nanocrystals formed in this confined thin film are unfaceted with a flattened spherical shape. We demonstrate that silicon atomic force microscope tips sliding over $CaSO_4$ crystals experience 40% lower friction and 70% lower wear compared to sliding directly on silicon.

---

* Corresponding author at: Advanced Research Center for Nanolithography (ARCNL), Science Park 106, 1098 XG Amsterdam, The Netherlands.
E-mail address: b.weber@arcnl.nl (B. Weber).

https://doi.org/10.1016/j.wear.2025.206457
Received 22 September 2025; Received in revised form 21 November 2025; Accepted 5 December 2025

2. Methods

2.1. Creation and removal of the deposit

As a substrate, we used polished, naturally oxidized, p-doped silicon wafers (University Wafer; <100> orientation; boron-doped; single-side polished; 500–525 μm thick; 1–10 Ω cm resistivity). We cut the wafers into pieces of approximately $2 \times 2\ \mathrm{cm}^2$. We cleaned the substrates by sequentially rinsing them with deionized water, hot tap water, ethanol, and deionized water again. We then plasma cleaned the samples for 10 min using oxygen gas in a Diener Electronic Zepto plasma cleaner. We placed a single $1\,\mu\mathrm{L}$ water droplet with a $CaSO_4$ concentration of $1.9\,\mathrm{g/L}$ on each plasma-cleaned sample. Upon evaporation – typically within about one minute at a relative humidity of 30–50% – the droplet left behind the $CaSO_4$ crystal deposit of interest on the surface.

2.2. Topography measurement

We performed topography measurements of the $CaSO_4$ deposit using both scanning electron microscopy (SEM; FEI Verios 460) and tapping mode atomic force microscopy (AFM; Bruker Dimension Icon and Bruker Innova).

2.3. Friction coefficient measurement

To compare the friction coefficients of the $CaSO_4$ crystals and uncoated silicon surfaces, we used lateral force microscopy (LFM) [28]. We acquired lateral deflection images that included both $CaSO_4$ crystals and the surrounding silicon wafer surface not covered by crystals. We subtracted the forward and backward scan directions to create friction coefficient maps. To calibrate the measured friction coefficients, we used the calibration method described by Varenberg et al. [29]. We applied this method to all three regions (the droplet edge, the transition region, and the precursor film of nanocrystals) of the deposited $CaSO_4$. In this way, we compared the friction coefficient of $CaSO_4$ crystals – ranging in size from $20\,\mathrm{nm}$ to 10 μm – to the smooth surface of naturally oxidized silicon. For these measurements, we used Bruker RESPA-20 and RESPA-10 model tips. On transition region bassanite crystals, we measured the friction coefficient at different contact pressures and at different relative humidities, to investigate how these factors influence the friction coefficient of both the crystals and the silicon substrate.

2.4. Tip wear measurement

In order to evaluate whether the nanocrystal deposit could protect a ceramic positioner surface from wear, we measured the wear rate of Bruker RTESPA 150 model silicon AFM tips when sliding against $CaSO_4$ crystals compared to sliding against uncoated p-type silicon wafers. We followed a protocol suited for wear tests on flat surfaces [30]; First, we performed repeated contact mode scans with a normal force of $100\,\mathrm{nN}$ over a $1 \times 1\ \mu\mathrm{m}^2$ area, which led to wear of a pyramidal section of the tip. We then imaged a Bruker RS-12M roughness sample using these degraded tips. The triangular base of the worn tip appeared as repeating features on the sample peaks. Using information on the shape of the AFM tip from the manufacturer [31] and from SEM images of the apex of the tip, we created a model to calculate the volume of the tip that has worn away using the size of the triangular base imprint. This derivation is provided in the Supplementary Information. Using this approach, we calculated the volume of the worn pyramid-shaped tip section and, from that, computed the average tip wear rate in $\mu\mathrm{m}^3/(\mathrm{Nm})$ for both uncoated silicon and the large gypsum crystals present at the *droplet edge*. Gypsum crystals were used in the wear experiments because these are the only $CaSO_4$ crystals large enough to accommodate the needed $1 \times 1\ \mu\mathrm{m}^2$ contact mode scan area.

2.5. Resilience of individual nanocrystals

Displacement of nanocrystals at frictional contacts may either accommodate relative motion (desirable) or cause contamination through nanocrystal redistribution (undesirable). To investigate the normal forces required to displace individual nanocrystals, we performed $3 \times 3\ \mu m^2$ contact mode AFM scans with normal forces ranging from 30 to 300 nN, followed by tapping mode topography imaging to assess the resulting nanocrystal displacement.

3. Results

3.1. Deposition morphology and zonal structure

We achieved dense and spatially extended nanocrystal deposits through droplet evaporation of aqueous $CaSO_4$, as shown in SEM and AFM scans in Fig. 1. The rapid evaporation at the droplet's edge generates a localized ion concentration gradient, prompting crystallization near the contact line. Nevertheless, crystal morphology varies significantly with location, allowing us to identify three distinct zones: a circular *droplet edge* that traces the initial three-phase contact line of the evaporated droplet (Fig. 1b); an intermediate *transition region* where the crystal size gradually decreases (Fig. 1c); and a homogeneous *nanocrystal deposit* extending outward from the edge (Fig. 1d). As our study focuses primarily on the nanocrystal region, we provide only a brief overview of the droplet edge and transition region here, with further details available in the Supplementary Information.

The structure of the droplet edge varied between and within samples. Some edges consisted of widely spaced gypsum crystals (Fig. 1b), while others featured a compact layer of fine bassanite crystals that completely covered the substrate (see Supplementary Information). At bassanite-rich edges, we observed a gradual reduction in nanocrystal size leading into the transition region (Fig. 1c), eventually merging with the amorphous nanocrystal zone (Fig. 1d). In contrast, gypsum-dominated edges exhibited abrupt transitions to the nanocrystal zone, with no intermediate-sized crystals (Figure S2). These differences arise because the low thickness of the liquid film near the droplet edge imposes geometric constraints on the crystalization of $CaSO_4$, with different polymorphs being favored depending on the size of the crystal that can form.

The homogeneous nanocrystal region extended at least $5\,\mathrm{cm}$ from the droplet edge with minimal variation in morphology or density (Figs. 1d and S5). AFM scans revealed that individual nanocrystals formed flattened spherical caps with heights of approximately $8\,\mathrm{nm}$ and lateral dimensions of $20\,\mathrm{nm}$ (Fig. 1e). Based on surface coverage analysis, we estimated that 1%–5% of the wafer area was directly covered by nanocrystals. Considering AFM tip convolution, we used 1% as a conservative estimate, corresponding to a number density of approximately $6 \times 10^{13}\ \mathrm{m}^{-2}$, or an average center-to-center spacing of roughly $125\,\mathrm{nm}$.

3.2. Mechanical stability and removability of the nanocrystal layer

To measure how firmly the nanocrystals adhere to the wafer surface, we performed contact-mode AFM scans with normal forces ranging from 30 to $300\,\mathrm{nN}$. We found that individual nanocrystals remained in place under forces up to approximately $30\,\mathrm{nN}$, but were displaced at higher loads. Phase contrast images (Figure S6b) confirmed that displaced nanocrystals left no detectable residue at their original locations. This could be explained by the unfaceted shape of the nanocrystals, allowing them to roll over the surface when force is applied.

Given the nanocrystal number density of $6 \times 10^{13}\ \mathrm{m}^{-2}$, we estimated that the deposit can withstand macroscopic pressures of up to $2\,\mathrm{MPa}$ before widespread nanocrystal displacement occurs (Figure S6). This threshold is substantially higher than the typical clamping pressures of $0.1\,\mathrm{MPa}$[37] used in vacuum chuck systems in the semiconductor

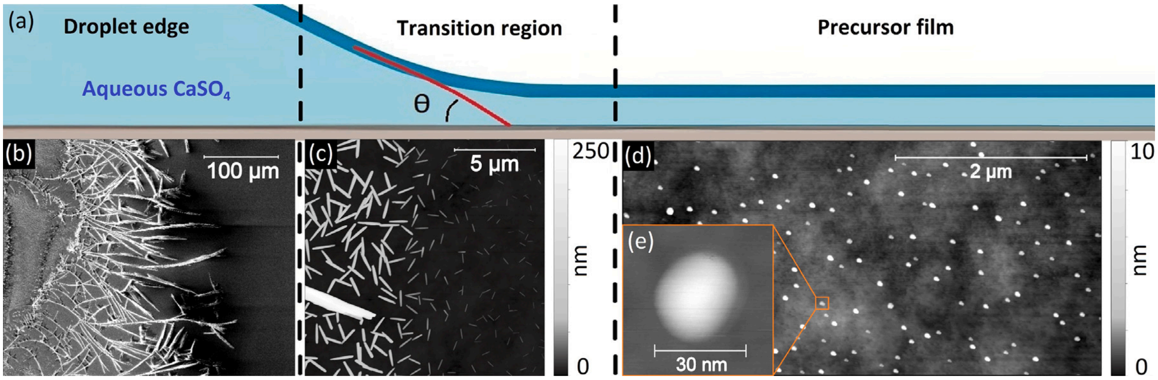

Fig. 1. (a) Schematic of a droplet of aqueous $CaSO_4$ solution evaporating on a silicon substrate, with a macroscopic contact angle $0° < \theta < 2°$ and a precursor film extending several centimeters from the droplet edge. Upon evaporation, three distinct deposition zones form, each characterized by different $CaSO_4$ morphologies. (b) SEM image of gypsum crystals ($CaSO_4{\cdot}2H_2O$) marking the former macroscopic contact line at the droplet edge. AFM images of (c) bassanite crystals ($CaSO_4{\cdot}\frac{1}{2}H_2O$) in the intermediate *transition region* between the droplet edge and the precursor film, (d) an amorphous nanocrystal deposit ($CaSO_4{\cdot}xH_2O$, water content $x > 0$ varies [32–36]) within the precursor film region, and (e) a close-up of an individual nanocrystal. Additional images are provided in the Supplementary Information.

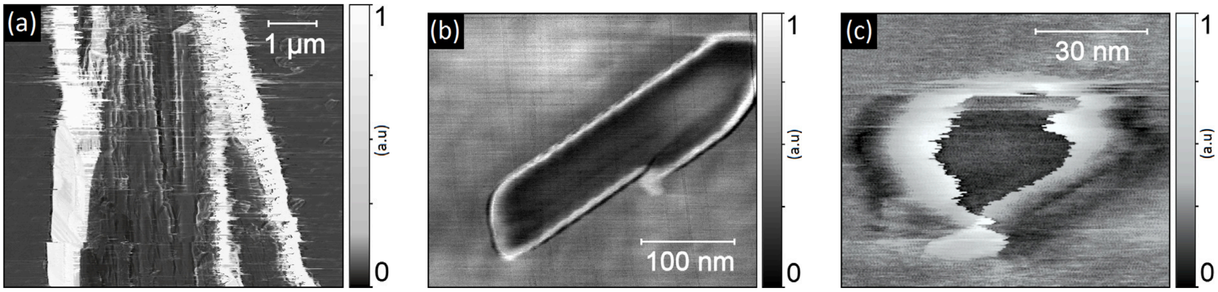

(a) (b) (c)

Fig. 2. Friction coefficient maps (in arbitrary units, a.u.) of three types of $CaSO_4$ deposits: (a) a gypsum crystal from the droplet edge, (b) a bassanite crystal from the transition region, and (c) an amorphous nanocrystal from the precursor film area. Note that slopes on the sample surfaces appear as high-friction artifacts. For all three types of crystal, the friction coefficient is about 0.4 on flat regions of the crystal and about 0.6 on flat regions of the silicon substrate (see also Figure S12).

industry, suggesting that the deposit may remain stable under practical conditions.

In addition, to test how easily the layer can be removed for cleaning purposes, we rinsed and immersed samples in distilled water. In all cases, the $CaSO_4$ layer dissolved completely within one minute, leaving no observable residue on the silicon surface (Figure S8). These results demonstrate that the nanocrystal deposit is both easy to create and easy to remove, which makes it attractive as a sacrificial spacer at (self-mated silicon) tribological interfaces.

3.3. Friction coefficients of $CaSO_4$ crystals and nanocrystals

In Fig. 2, lateral force microscopy (LFM) maps of three types of $CaSO_4$ morphologies are presented: (i) large gypsum crystals at the droplet edge (Fig. 2a), (ii) bassanite crystals in the transition region (Fig. 2b), and (iii) amorphous nanocrystals from the precursor film region (Fig. 2c).

Each LFM pixel intensity reflects the lateral force measured at that point. Boundaries of individual crystals appear as high-friction zones because the tip experiences resistance as it climbs on top the crystal. The friction coefficient of the large gypsum crystal is strongly variable. On flat regions the friction coefficient is lower than on the surrounding silicon, just like for nanoparticles and bassanite crystals, but in many other places it is much higher. This can be attributed to the high surface roughness of large gypsum crystals in comparison to both uncoated silicon and the other types of $CaSO_4$ crystals. By comparing the average friction on top of the crystals with the average values outside the crystals, we estimate the ratio of the friction coefficient of silicon and the three types of CaSO4 crystals. In this way, we find that the friction coefficient of $CaSO_4$ nanoparticles and larger bassanite crystals is approximately 40% lower than that of the surrounding uncoated silicon. We repeated the friction measurements on bassanite crystals using calibrated AFM tips at varying normal force and varying relative humidity (Fig. S12), thereby showing that the friction coefficient on bassanite is 0.38±0.06, independent of humidity, while the friction coefficient measured on bare silicon increases from 0.52±0.07 to 0.60±0.07 as the humidity is raised from 6% to 60%. Furthermore, by varying the normal force, we observed a modest but not statistically significant reduction in friction coefficient with increasing normal force, which is likely caused by adhesion. Finally, we note that the contact forces exerted in our experiment result in contact pressures ranging from 1-2 GPa, according to Hertz theory, while the shear stresses are approximately half. Overall, our observations suggests that the nanoparticle deposit effectively reduces the friction coefficient of the silicon surface to which it is applied.

3.4. AFM tip wear on silicon and gypsum crystals

To quantify the degree to which the $CaSO_4$ deposits can suppress silicon-on-silicon wear, we performed controlled wear experiments (see Methods, Fig. 3 and Table 1) both on gypsum crystals located at the droplet edge (Fig. 1b) and on uncoated silicon wafers.

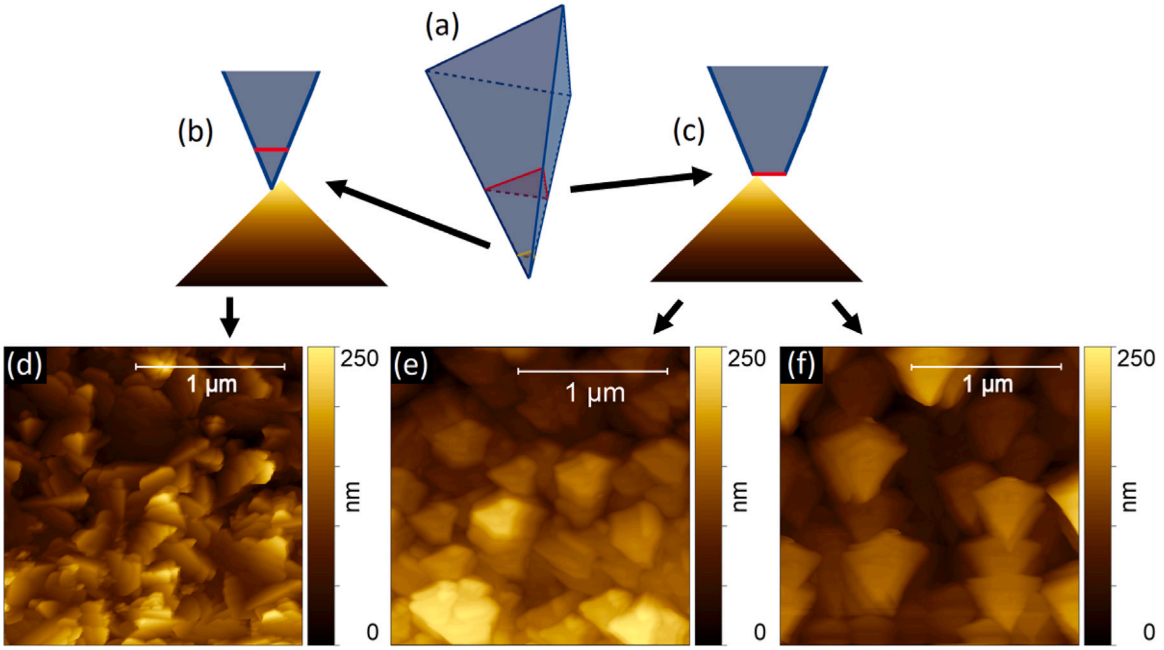

Fig. 3. Procedure used to estimate the worn volume of an AFM tip. (a) Model of the RTESPA-150 tip used in experiments. As the tip slides over a flat surface, material is gradually removed from the apex, exposing a triangular cross-section that increases in size with wear—starting small (yellow surface) and growing larger (red surface). (b,c) Schematics of a lightly worn tip (b) and a heavily worn tip (c) scanning a sharp feature of the reference roughness sample. Because the sample features are sharper than the worn tips, the resulting images effectively demonstrate the geometry of the degraded tip. (d–f) Scans of the Bruker RS-12M roughness sample acquired using (d) a fresh tip, (e) a tip worn on gypsum, and (f) a tip worn on silicon. The size of the exposed triangular cross-section is extracted from these images, and the corresponding wear volume is calculated. Additional details are provided in the Supplementary Information (Figures S9 and S10).

The measured silicon-on-silicon wear rate agrees with previous measurements of silicon wear under self-mated and ambient conditions [38], thereby providing independent support for our methodology. On average, the tip wear rate was 70% lower when scanning over gypsum (1.9×10^5 $\mu m^3/(N\ m)$) compared to silicon (7.0×10^5 $\mu m^3/(N\ m)$). This suggests that the nanoparticle deposit can indeed significantly reduce wear of surfaces sliding against a silicon sample, as may be expected based on the lower hardness of gypsum [23,24] compared to silicon. Individual measurements on gypsum exhibited higher uncertainty due to irregular wear profiles on rough crystal surfaces, whereas scans on smooth silicon showed less variation in average wear rate. Finally, it should be noted that at the start of each wear test, the contact stress is about 1 GPa. As the tip wear progresses, the contact stress is expected to decrease substantially, which may in turn reduce the wear rate.

Table 1

Summary of the wear rate of uncoated silicon AFM tips sliding over either uncoated silicon wafers or gypsum crystals. The wear rate on softer [23,24] gypsum is substantially lower than on harder [4] silicon.

Results of tip wear rate experiments on silicon and gypsum crystals		
	Si wafer	Gypsum crystal
Contact force (nN)	100	100
Number of measurements	5	10
Scan distances (mm)	5–102	3–240
Average wear rate (10^5 $\mu m^3/(N\ m)$)	7.0	1.9
Minimum and maximum wear rate (10^5 $\mu m^3/(N\ m)$)	4.4–10.0	0.16–6.2
Uncertainty per measurement (%)	30	70
Uncertainty of average result (%)	14	22

4. Discussion

4.1. Nanocrystal distribution and interfacial applications

The investigated nanocrystal deposit remains morphologically consistent over several centimeters, confirming the uniformity and scalability of the deposition approach. This uniformity makes the deposit a promising candidate for use as a sacrificial interfacial layer in applications that require nanoscale separation between flat surfaces—such as between silicon wafer backsides and positioners in semiconductor equipment. The measured height and lateral dimensions of the nanocrystals are sufficient to maintain a controlled separation, potentially reducing direct contact and the resulting friction and wear in precision positioning systems.

Based on morphological comparison with literature [32,33], we attribute the deposited nanocrystals to quasi spherical amorphous calcium sulfate, and the nanorod shapes to bassanite ($CaSO_4\cdot\frac{1}{2}H_2O$). The amorphous character may offer mechanical compliance and low adhesion, facilitating easy removal and minimizing contamination. These features could support the development of reversible surface separation strategies in cleanroom environments.

4.2. Stability and reversibility of the nanocrystal layer

We found that individual nanocrystals withstand normal forces of up to approximately 30 nN, corresponding to a macroscopic pressure of about 2 MPa. This value exceeds the typical clamping pressures of 0.1 MPa[37] used in vacuum chuck systems, indicating that the deposit remains stable under standard operating conditions in semiconductor processing.

We also confirmed that the layer can be fully removed by simple rinsing or brief immersion in distilled water, without leaving detectable residues. This ease of removal highlights the reversibility of the deposition and supports its suitability as a temporary or disposable interfacial layer.

4.3. Friction reduction and morphology effects

Our lateral force microscopy measurements showed that both amorphous $CaSO_4$ nanocrystals and bassanite nanorod crystals reduce local friction coefficients by approximately 40% compared to the surface of the bare silicon. This reduction is especially valuable in precision positioning systems, where friction-induced microdeformation and wear can degrade performance [39].

In contrast, larger gypsum crystals exhibited spatially heterogeneous friction behavior due to their faceted shape. In flat regions, friction was relatively low, but in rougher areas, friction values were significantly higher. We attribute this variation to increased local asperities and topographical irregularities. These results suggest that smoother morphologies, such as the quasi-spherical amorphous nanocrytals and nanorods of bassanite, offer more consistent and predictable frictional behavior, making them better suited for integration into precision tribological systems.

4.4. Wear reduction on gypsum surfaces

Our AFM tip wear experiments demonstrated that sliding on gypsum crystals reduced tip wear rates by approximately 70% compared to sliding on silicon. Despite the relatively rough surface of gypsum, this protective effect was consistently observed across multiple measurements.

This finding is significant for applications where uncoated silicon components undergo repeated sliding, such as in micro-positioning stages or MEMS devices. Reducing tip or surface wear with $CaSO_4$ deposits could extend component lifetimes and improve reliability.

While tip wear measurements on gypsum showed higher uncertainty due to irregular wear geometries, the overall trend remains robust. The smoother surface of silicon allowed for more precise volume loss measurements and served as a reliable baseline for comparison. These results support the concept that sacrificial or compliant surface layers can mitigate wear in silicon-on-silicon contact scenarios.

4.5. Outlook

We have shown that $CaSO_4$ nanocrystals offer favorable friction and wear properties at the single-nanocrystal level. However, practical implementations will involve larger contact areas where many nanocrystals simultaneously contribute to interfacial behavior. A natural next step is to conduct macroscale friction experiments – such as wafer-on-wafer contact tests – to determine whether these beneficial effects persist at larger scales.

We selected $CaSO_4$ for this study due to its previously reported ability to form stable nanocrystals during evaporation [25,32,33]. However, we see no fundamental reason to assume that $CaSO_4$ performs better than other low solubility salts. Since the deposition method is general, future work could explore analogous deposits formed from other salt systems, particularly those already reported in literature [27]. Furthermore, the influence of other deposition methods or drying conditions could be studied.

5. Conclusion

We demonstrated that droplet-based nanocrystal deposition offers a simple and effective method to form dense and spatially uniform nanocrystal layers on silicon wafers. These layers span several centimeters with consistent morphology and coverage, enabling their potential use as sacrificial interfacial coatings in flat-on-flat contact applications.

We characterized the deposited nanocrystals as quasi spherical amorphous calcium sulfate with average dimensions of approximately 8 nm in height and 20 nm in lateral diameter. The nanocrystals remained mechanically stable under normal forces up to 30 nN, corresponding to a macroscopic pressure of about 2 MPa, well above the pressures used in vacuum chuck systems. Additionally, the entire deposit could be removed easily by rinsing with water, leaving no observable residue.

Through lateral force microscopy, we found that both amorphous nanocrystals and bassanite crystals reduced surface friction by approximately 40% compared to bare silicon. Wear tests using silicon AFM tips revealed a 70% reduction in tip wear when sliding over gypsum crystals relative to silicon, further underscoring the deposit's protective potential.

Together, these findings indicate that $CaSO_4$ nanocrystal layers can reduce friction and wear at critical ceramic interfaces, such as those found in semiconductor positioning systems. Their ease of application, reversibility, and tribological performance make them promising candidates for integration into cleanroom-compatible, precision-engineered surfaces.

CRediT authorship contribution statement

Tijn Vernooij: Writing – review & editing, Writing – original draft, Visualization, Software, Methodology, Investigation, Formal analysis, Data curation, Conceptualization. **H. Tunç Çiftçi:** Writing – review & editing, Supervision, Methodology, Investigation, Conceptualization. **Noushine Shahidzadeh:** Writing – review & editing, Validation, Supervision, Resources, Methodology, Formal analysis, Conceptualization. **Bart Weber:** Writing – review & editing, Supervision, Resources, Project administration, Methodology, Conceptualization.

Declaration of competing interest

The authors declare that they have no known competing financial interests or personal relationships that could have appeared to influence the work reported in this paper.

Acknowledgments

This work was conducted at the Advanced Research Center for Nanolithography, a public–private partnership between the University of Amsterdam (UvA), Vrije Universiteit Amsterdam (VU), Rijksuniversiteit Groningen (RUG), the Netherlands Organization for Scientific Research (NWO), and the semiconductor equipment manufacturer ASML. We thank Ozan Sahin for making high-resolution SEM images of one of our samples. These images are used in Fig. 1 and Figure S2 of the Supplementary Information.

Appendix A. Supplementary data

Supplementary material related to this article can be found online at https://doi.org/10.1016/j.wear.2025.206457.

Data availability

Data will be made available on request.

References

[1] W. Gao, S. Kim, H. Bosse, H. Haitjema, Y. Chen, X. Lu, W. Knapp, A. Weckenmann, W. Estler, H. Kunzmann, Measurement technologies for precision positioning, CIRP Ann 64 (2) (2015) 773–796.

[2] T. Oiwa, M. Katsuki, M. Karita, W. Gao, S. Makinouchi, K. Sato, Y. Oohashi, Questionnaire survey on ultra-precision positioning, Int. J. Autom. Technol. 5 (6) (2011) 766–772.

[3] Substrate holder and a method of manufacturing a substrate holder, 2017, US Patent US10719019B2.

[4] C. Leriche, C. Xiao, S. Franklin, B. Weber, From atomic attrition to mild wear at multi-asperity interfaces: The wear of hard Si3N4 repeatedly contacted against soft Si, Wear 528–529 (2023) 204975.

[5] E. Medvedovski, Engineering ceramics for wear-protection of mining and mineral processing equipment, 2018, pp. 647–651.

[6] X.S. Li, I.M. Low, Ceramic cutting tools-an introduction, Key Eng. Mater. 96 (1994) 1–18.
[7] H. Bhaskaran, B. Gotsmann, A. Sebastian, U. Drechsler, M. Lantz, M. Despont, P. Jaroenapibal, R. Carpick, Y. Chen, K. Sridharan, Ultralow nanoscale wear through atom-by-atom attrition in silicon-containing diamond-like carbon, Nature Nanotechnology 5 (2010) 181–185.
[8] G. Roscioli, S.M. Taheri-Mousavi, C.C. Tasan, How hair deforms steel, Science 369 (6504) (2020) 689–694.
[9] C. Leriche, E. Pedretti, O. Sahin, D. Kang, M.C. Righi, B. Weber, Passivation species suppress atom-by-atom wear of microcrystalline diamond, ACS Appl. Mater. Interfaces 17 (39) (2025) 55511–55520, PMID: 40965355.
[10] J. Desarnaud, D. Bonn, S. Noushine, Measurement of the pressure induced by salt crystallization in confinement, Sci. Rep. 6 (2016).
[11] R.A. Wüst, C. Schlüchter, The origin of soluble salts in rocks of the thebes mountains, Egypt: The damage potential to ancient Egyptian wall art, J. Archaeol. Sci. 27 (12) (2000) 1161–1172.
[12] A. Hamilton, V. Koutsos, C. Hall, Direct measurement of salt-mineral repulsion using atomic force microscopy, Chem. Commun. (Cambridge, England) 46 (2010) 5235–5237.
[13] E.M. Winkler, P.C. Singer, Crystallization pressure of salts in stone and concrete, GSA Bull. 83 (11) (1972) 3509–3514.
[14] H. Shindo, S.-i. Kondo, K. Shitagami, T. Sugai, Y. Namai, M. Kwak, Frictional force microscopic detection of anisotropy and asymmetry at various atom-flat surfaces, in: World Tribology Congress III, Volume 2, in: World Tribology Congress, 2005, pp. 729–730.
[15] A. Socoliuc, R. Bennewitz, E. Gnecco, E. Meyer, Transition from stick-slip to continuous sliding in atomic friction: Entering a new regime of ultralow friction, Phys. Rev. Lett. 92 (2004) 134301.
[16] J.-W. Kim, J.-H. Ree, R. Han, T. Shimamoto, Experimental evidence for the simultaneous formation of pseudotachylyte and mylonite in the brittle regime, Geology 38 (2010) 1143–1146.
[17] H.-G. Wang, B. Mu, J.-F. Ren, L.-Q. Jian, J.-Y. Zhang, S.-R. Yang, Mechanical and tribological behaviors of PA66/PVDF blends filled with calcium sulphate whiskers, Polym. Compos. 30 (9) (2009) 1326–1332.
[18] J. Sudhan Raj, T. Christy, S. Darius Gnanaraj, B. Sugozu, Influence of calcium sulfate whiskers on the tribological characteristics of automotive brake friction materials, Eng. Sci. Technol. an Int. J. 23 (2) (2020) 445–451.
[19] P. John, S. Prasad, A. Voevodin, J. Zabinski, Calcium sulfate as a high temperature solid lubricant, Wear 219 (2) (1998) 155–161.
[20] P.J. John, J.S. Zabinski, Sulfate based coatings for use as high temperature lubricants, Tribol. Lett. 7 (1) (1999) 31–37.
[21] T. Yamamoto, M. Olsson, S. Hogmark, Three-body abrasive wear of ceramic materials, Wear 174 (1) (1994) 21–31.
[22] Y. Wang, S.M. Hsu, Wear and wear transition mechanisms of ceramics, Wear 195 (1) (1996) 112–122.
[23] M.E. Broz, R.F. Cook, D.L. Whitney, Microhardness, toughness, and modulus of Mohs scale minerals, Am. Mineral. 91 (1) (2006) 135–142.
[24] J. Zhou, C. Liu, Z. Shu, D. Yu, Q. Zhang, T. Li, Q. Xue, Preparation of specific gypsum with advanced hardness and bending strength by a novel in-situ loading-hydration process, Cem. Concr. Res. 67 (2015) 179–183.
[25] N. Shahidzadeh-Bonn, M.F. Schut, J. Desarnaud, M. Prat, D. Bonn, Salt stains from evaporating droplets, Sci. Rep. 5 (2015) 1–9.
[26] M.N. Popescu, G. Oshanin, S. Dietrich, A.-M. Cazabat, Precursor films in wetting phenomena, J. Phys.: Condens. Matter. 24 (24) (2012) 243102.
[27] M.J. Qazi, H. Salim, C.A.W. Doorman, E. Jambon-Puillet, N. Shahidzadeh, Salt creeping as a self-amplifying crystallization process, Sci. Adv. 5 (12) (2019) eaax1853.
[28] M. Reitsma, R. Cain, D. Smith, S. Biggs, N. Page, Lateral force microscopy: A tool for tribology, GeoEng 2000 Conf. (2000).
[29] M. Varenberg, I. Etsion, G. Halperin, An improved wedge calibration method for lateral force in atomic force microscopy, Rev. Sci. Instrum. 74 (2003) 3362–3367.
[30] E.E. Flater, J.D. Barnes, J.A. Hitz Graff, J.M. Weaver, N. Ansari, A.R. Poda, W. Robert Ashurst, S.R. Khanal, T.D.B. Jacobs, A simple atomic force microscope-based method for quantifying wear of sliding probes, Rev. Sci. Instrum. 89 (11) (2018) 113708.
[31] Bruker AFM Probes - RTESPA-150. URL https://www.brukerafmprobes.com/p-3911-rtespa-150.aspx.
[32] Y.-W. Wang, H.K. Christenson, F.C. Meldrum, Confinement leads to control over calcium sulfate polymorph, Adv. Funct. Mater. 23 (45) (2013) 5615–5623.
[33] Y.-W. Wang, Y.-Y. Kim, H.K. Christenson, F.C. Meldrum, A new precipitation pathway for calcium sulfate dihydrate (gypsum) via amorphous and hemihydrate intermediates, Chem. Commun. 48 (2012) 504–506.
[34] A.E.S.V. Driessche, L.G. Benning, J.D. Rodriguez-Blanco, M. Ossorio, P. Bots, J.M. García-Ruiz, The role and implications of bassanite as a stable precursor phase to gypsum precipitation, Science 336 (6077) (2012) 69–72.
[35] A. Saha, J. Lee, S.M. Pancera, M.F. Bräeu, A. Kempter, A. Tripathi, A. Bose, New insights into the transformation of calcium sulfate hemihydrate to gypsum using time-resolved cryogenic transmission electron microscopy, Langmuir 28 (30) (2012) 11182–11187, PMID: 22747102.
[36] C. Jia, L. Wu, J.L. Fulton, X. Liang, J.J. De Yoreo, B. Guan, Structural characteristics of amorphous calcium sulfate: Evidence to the role of water molecules, J. Phys. Chem. C 125 (6) (2021) 3415–3420.
[37] J. van Elp, P. Giesen, A. de Groof, Low-thermal expansion electrostatic chuck materials and clamp mechanisms in vacuum and air, Microelectron. Eng. 73–74 (2004) 941–947, Micro and Nano Engineering 2003.
[38] F.-C. Hsia, C.-C. Hsu, L. Peng, F.M. Elam, C. Xiao, S. Franklin, D. Bonn, B. Weber, Contribution of capillary adhesion to friction at macroscopic solid–solid interfaces, Phys. Rev. Appl. 17 (2022) 034034.
[39] S. Thiery, M. Kunze, A. Karimi, A. Curnier, R. Longchamp, Friction modeling of a high-precision positioning system, vol. 2006, 2006, p. 5.